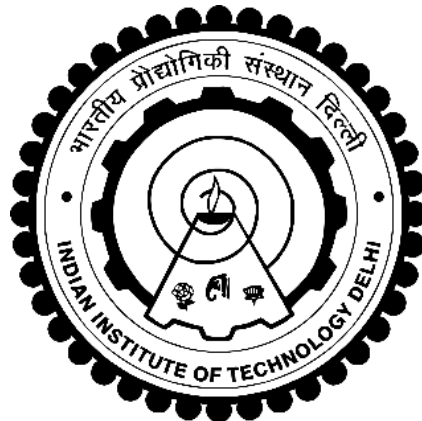


**NANOMECHANICS OF *BOMBYX MORI* SILK FIBROIN-  
HYDROXYAPATITE NANOCOMPOSITE USING MOLECULAR  
DYNAMICS SIMULATIONS**

**MRINAL PATEL**



**DEPARTMENT OF MECHANICAL ENGINEERING  
INDIAN INSTITUTE OF TECHNOLOGY DELHI  
SEPTEMBER 2022**

© Indian Institute of Technology Delhi (IITD), New Delhi, 2022

**NANOMECHANICS OF *BOMBYX MORI* SILK FIBROIN-  
HYDROXYAPATITE NANOCOMPOSITE USING MOLECULAR  
DYNAMICS SIMULATIONS**

*by*

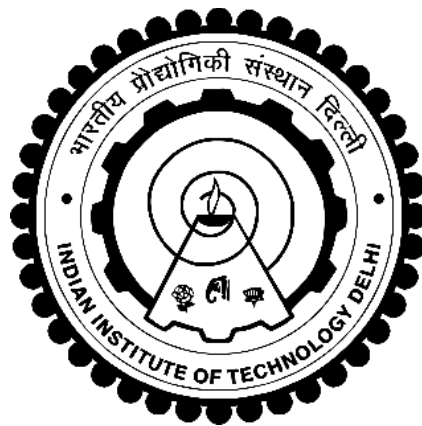
**MRINAL PATEL**

**DEPARTMENT OF MECHANICAL ENGINEERING**

submitted in fulfilment of the requirements for the degree of

**DOCTOR OF PHILOSOPHY**

*to the*



**INDIAN INSTITUTE OF TECHNOLOGY DELHI**

**NEW DELHI-110016, INDIA**

**SEPTEMBER 2022**

## CERTIFICATE

This is to certify that the thesis entitles, “**Nanomechanics of *Bombyx Mori* Silk Fibroin-Hydroxyapatite Nanocomposite using Molecular Dynamics Simulations**”, being submitted by **Mrinal Patel** to the Indian Institute of Technology Delhi, New Delhi, for the award of the degree of **Doctor of Philosophy in Mechanical Engineering** is a record of bonafide research work carried out by her under my supervision and guidance. She has fulfilled the requirement for the submission of the thesis, which to the best of my knowledge has reached the requisite standard.

The material contained in the thesis has not been submitted in part or full to any other University or Institute for the award of any degree or diploma.

Prof. S. P. Singh

Professor

Thesis Supervisor

Department of Mechanical Engineering

Indian Institute of Technology Delhi

Hauz Khas New Delhi 110016

Prof. Devendra Dubey

Assoc. Professor

Thesis Supervisor

Department of Mechanical Engineering

Indian Institute of Technology Delhi

Hauz Khas New Delhi 110016

## ACKNOWLEDGEMENTS

I would like to humbly acknowledge my advisors Prof. S. P. Singh and Prof. Devendra Kumar Dubey for their continuous support and motivation during my duration of doctoral research at IIT Delhi. I am very grateful for being under the guidance of such kind, humble, creative personalities who always encouraged me during demanding situation during the research. I have learned a lot from them. I would also like to thank members of my dissertation committee, Prof. J. K. Dutt, Prof. Naresh Verma Datla, and Prof. Sourabh Ghosh for their valuable and critical comments which really helped me to improve the quality of work.

To achieve the final goal of doctoral thesis the pathways had many peaks and valleys. The rigorous period of research would not have been bearable without the support of beloved friends and colleagues Mr. Abhinava Chatterjee, Mr. Shambo Bhattacharya, Mrs. Rachna Joshi, Mr. Chandra Shekhar and Mr. Rohit Sankrityayan. Their constant support kept me moving on the right track. I would like to thanks to all the members and admin of CAGI Lab for their help, constant support and a healthy discourse.

Faculty members of IIT Delhi who have played a major role in my journey at IIT Delhi. I would like to thank specially Prof. S. K. Saha (Ex-HOD Mechanical Engineering Department), and Prof. M.R. Ravi (Current HOD) for their valuable suggestions. I would like to thank the efforts of staff of Department of Mechanical Engineering, Computer Service center for availing the facility of HPC which played a crucial role in my research.

I am very fortunate for being blessed with parents (Mr. Jogendra Kumar and Mrs. Usha Patel) and husband (Mr. Harshit Gupta) who have always motivated me and encouraged for an affirmative action during tough times. Lastly, I would like to express my greatest gratitude to the God Almighty for being a source of constant hope and energy to achieve new heights in personal and career development.

## Abstract

Silk Fibroin-hydroxyapatite (SF-HAP) bio-nanocomposite is a prospective biomaterial for tissue engineered graft or scaffold for bone repair. Here, SF is primarily a soft, organic phase and HAP is a stiffer, mineral phase. Silk fibers, majorly produced by silkworms (e.g. *Bombyx mori*), is a promising biopolymer for use in biomedical applications such as tissue engineered grafts as it is a load bearing biopolymer with biocompatible and bioresorbable properties. *Bombyx mori* Silk Fibroin (*B. mori* SF) is a hierarchical bio-macro-molecule made up of amino acid residues consisting of crystalline phase and amorphous phases. Understanding about the mechanical behavior of *B. mori* SF at multiple length scales is of importance when developing tissue grafts, which requires a deeper understanding of deformation behavior and involved molecular mechanisms at nanoscale. Along with the mechanical behavior of *B. mori* SF, the interfacial interaction between SF and HAP also, is a defining factor for the mechanical performance of SF-HAP bio-nanocomposite. To investigate such nanoscale behavior, molecular dynamics (MD) method is a preferred approach. This study focuses on understanding of the mechanical properties and deformation mechanism of *B. mori* SF at nanometer length scale, considering the effect of structural aspects and chemical environment. For this purpose, phenomenological atomistic models of *B. mori* SF nanostructures are developed, based on connectivity and relative arrangement of crystalline and amorphous domains. Tensile loading based mechanical behavior analyses of these *B. mori* SF models were performed using MD simulations and compared with existing results from literature. Elastic modulus of  $\sim 7.4 \pm 0.3$  GPa and tensile strength of  $\sim 340 \pm 20$  MPa were obtained for this model. Analysis of results reveals that deformation mechanisms in *B. mori* SF at nanoscale are a combination of tensile and shear deformations, wherein, the deformation of *B. mori* SF nanostructure starts with tensile deformation of amorphous chains (mainly), followed by also shear distortion of crystallites (along with tensile deformation of amorphous chains) at high strain values. The shear distortion of crystalline region is correlated with the strain hardening and peak stress value observed during tensile deformation of *B. mori* SF nanostructure. In addition, the tensile deformation of amorphous chains defines the high extension observed in *B. mori* SF nanostructure during tensile deformation, whereas, shear distortion of crystalline region defines the high tensile strength. Moreover, current study also focuses on the role of interfacial interaction between SF and HA in overall mechanical behavior of

SF-HA bio-nanocomposite. For this purpose, SF-HA interface models based on HA crystal size and HA surface in contact with SF has been developed. Pull-out tests are performed to analyze the interface debonding behavior of these SF-HA interface models using Steered Molecular Dynamics (SMD) simulations. Current work contributes in developing an understanding of mechanistic interactions between amorphous and crystalline domains in *B. mori* SF nanostructure and between the protein and mineral phases in SF-HA bio-nanocomposite.

## सार

सिल्क फाइब्रोइन-हाइड्रॉक्सीपैटाइट (एसएफ- एचए) बायो-नैनोकंपोजिट हड्डी की मरम्मत के लिए ऊतक इंजीनियर ग्राफ्ट या मचान के लिए एक संभावित बायोमटेरियल है। यहां, SF मुख्य रूप से एक नरम, जैविक अवस्था है और एचए एक कठोर, खनिज अवस्था है। सिल्क फाइबर (जैसे बॉम्बेक्स मोरी) द्वारा प्रमुख रूप से उत्पादित रेशम फाइबर, ऊतक इंजीनियर ग्राफ्ट जैसे जैव चिकित्सा अनुप्रयोगों में उपयोग के लिए एक आशाजनक बायोपॉलिमर है क्योंकि यह बायोकंपैटिबल और बायोरेसोरेबल गुणों के साथ एक भार वहन करने वाला बायोपॉलिमर है। बॉम्बेक्स मोरी सिल्क फाइब्रोइन (बी मोरी एसएफ) एक पदानुक्रमित जैव-मैक्रो-अणु है जो क्रिस्टलीय चरण और अनाकार चरणों से युक्त अमीनो एसिड अवशेषों से बना होता है। ऊतक ग्राफ्ट विकसित करते समय कई लंबाई के पैमाने पर बी मोरी एसएफ के यांत्रिक व्यवहार के बारे में समझना महत्वपूर्ण है, जिसके लिए नैनोस्केल पर विरूपण व्यवहार और शामिल आणविक तंत्र की गहरी समझ की आवश्यकता होती है। बी. मोरी एसएफ के यांत्रिक व्यवहार के साथ-साथ, एसएफ और एचएपी के बीच पारस्परिक संपर्क भी, एसएफ-एचएपी जैव-नैनोकंपोजिट के यांत्रिक प्रदर्शन के लिए एक परिभाषित कारक है। ऐसे नैनोस्केल व्यवहार की जांच करने के लिए, आणविक गतिकी (एमडी) विधि एक पसंदीदा तरीका है। यह अध्ययन संरचनात्मक पहलुओं और रासायनिक वातावरण के प्रभाव पर विचार करते हुए नैनोमीटर लंबाई के पैमाने पर बी मोरी एसएफ के यांत्रिक गुणों और विरूपण तंत्र की समझ पर केंद्रित है। इस उद्देश्य के लिए, क्रिस्टलीय और अनाकार डोमेन की कनेक्टिविटी और सापेक्ष व्यवस्था के आधार पर, बी मोरी एसएफ नैनोस्ट्रक्चर के घटनात्मक परमाणु मॉडल विकसित किए गए हैं। इन बी मोरी एसएफ मॉडल के तन्य लोडिंग आधारित यांत्रिक व्यवहार विश्लेषण एमडी सिमुलेशन का उपयोग करके और साहित्य से मौजूदा परिणामों की तुलना में किए गए थे। इस मॉडल के लिए  $\sim 7.4 \pm 0.3$  GPa का लोचदार मापांक और  $\sim 340 \pm 20$  MPa की तन्यता ताकत प्राप्त की गई थी। परिणामों के विश्लेषण से पता चलता है कि नैनोस्केल पर बी मोरी एसएफ में विरूपण तंत्र तन्यता और कतरनी विकृतियों का एक संयोजन है, जिसमें, बी मोरी एसएफ नैनोस्ट्रक्चर का विरूपण अनाकार श्रृंखला (मुख्य रूप से) के तन्य विरूपण के साथ शुरू होता है, इसके बाद कतरनी विरूपण भी होता है। उच्च तनाव मूल्यों पर क्रिस्टलीय (अनाकार श्रृंखलाओं के तन्य विरूपण के साथ)। क्रिस्टलीय क्षेत्र का अपरूपण विरूपण बी मोरी एसएफ नैनोस्ट्रक्चर के तन्य विरूपण के दौरान देखे गए तनाव सख्त और शिखर तनाव मूल्य के साथ सहसंबद्ध है। इसके अलावा, अनाकार श्रृंखलाओं का तन्य विरूपण तन्यता विरूपण के दौरान बी मोरी एसएफ नैनोस्ट्रक्चर में देखे गए उच्च विस्तार को परिभाषित करता है, जबकि, क्रिस्टलीय क्षेत्र का कतरनी विरूपण उच्च तन्यता ताकत को परिभाषित करता है। इसके अलावा, वर्तमान अध्ययन एसएफ-एचए बायो-नैनोकंपोजिट के समग्र यांत्रिक व्यवहार में एसएफ और एचए के बीच पारस्परिक संपर्क की भूमिका पर भी केंद्रित है। इस प्रयोजन के

लिए, एसएफ़ के संपर्क में एचए क्रिस्टल आकार और एचए सतह पर आधारित एसएफ़-एचए इंटरफ़ेस मॉडल विकसित किए गए हैं। स्टीयरिंग मॉलिक्यूलर डायनेमिक्स (SMD) सिमुलेशन का उपयोग करके इन एसएफ़-एचए इंटरफ़ेस मॉडल के इंटरफ़ेस डिबॉन्डिंग व्यवहार का विश्लेषण करने के लिए पुल-आउट परीक्षण किए जाते हैं। वर्तमान कार्य बी मोरी एसएफ़ नैनोस्ट्रक्चर में अनाकार और क्रिस्टलीय डोमेन के बीच और एसएफ़-एचए बायो-नैनोकंपोजिट में प्रोटीन और खनिज चरणों के बीच यंत्रवत बातचीत की समझ विकसित करने में योगदान देता है।

# Table of Contents

Certificate	
Acknowledgements	
Abstract	
Table of Contents	
List of Figures	
List of Tables	
<b>1. Introduction</b> .....	<b>1</b>
1.1. Motivation.....	1
1.2. Silk as a biomaterial.....	2
1.2.1. Hierarchical Structure of Silk.....	3
1.3. Silk-Hydroxyapatite biomaterial for bone tissue engineering.....	6
<b>2. Literature Review</b> .....	<b>8</b>
2.1. Studies on structural investigation and mechanical behavior of <i>B. mori</i> SF.....	8
2.2. Studies on mechanical behavior of <i>B. mori</i> SF-HA bio-nanocomposites.....	12
2.3. Conclusions from literature review.....	13
2.4. Objectives of thesis.....	14
<b>3. Atomistic model of <i>B. mori</i> SF Nanostructure and deformation mechanism under tensile loading</b> .....	<b>16</b>
3.1. Structure of <i>B. mori</i> SF.....	17
3.2. Atomistic Models of <i>B. mori</i> SF.....	19
3.2.1. Modelling of Crystalline and Amorphous regions.....	19
3.2.2. Computational Model of <i>B. mori</i> SF nanostructure.....	21
3.3. Simulation Details.....	24
3.4. Results and Discussion.....	30
3.4.1. Stress-Strain Behavior of <i>B. mori</i> SF Models.....	30
3.4.2. Elastic Regime.....	37
3.4.3. Strain Softening Regime.....	39
3.4.4. Strain Hardening Regime.....	42
3.4.5. Strain Rate Effect.....	49

3.4.6. Size Effect.....	52
3.5. Summary and Conclusions.....	56
<b>4. Effect of varying hydration conditions on mechanical behavior and deformation mechanism of <i>B. mori</i> SF Nanostructure.....</b>	<b>58</b>
4.1. Computational Model of <i>B. mori</i> SF Nanostructure.....	59
4.2. Simulation Details.....	62
4.3. Results and Discussion.....	67
4.3.1. Effect of Hydration on Stress-Strain Behavior of <i>B. mori</i> SF.....	68
4.3.2. Role of H-bonds Interactions in <i>B. mori</i> SF Nanomechanics.....	76
4.3.3. Role of Bonded and Non-Bonded Energies in <i>B. mori</i> SF nanomechanics.....	78
<i>Potential Energy of the Polypeptide</i> .....	79
<i>Role of Peptide-Peptide and Peptide-Water Interactions</i> .....	80
4.4. Summary and Conclusions.....	84
<b>5. Nano-mechanical behavior of <i>B. mori</i> SF under Saline Environment.....</b>	<b>87</b>
5.1. Atomistic Computational Model of <i>B. mori</i> SF Nanostructure.....	88
5.2. Simulation Details.....	90
5.3. Results and Discussion.....	93
5.3.1. Effect of Salt Concentration on Stress-Strain Behavior and Tensile Properties.....	93
5.3.2. Molecular Flow Behaviour of <i>B. mori</i> SF in Saline Environment under Tensile Deformation.....	99
5.3.3. Role of Peptide-Peptide Non-Bonded Interactions.....	101
5.3.4. Role of Peptide-Salt Interactions.....	102
5.4. Summary and Conclusions.....	114
<b>6. Nanomechanics and mechanical deformation behavior of <i>B. mori</i> SF under dynamic loading.....</b>	<b>116</b>
6.1. Simulation Details.....	117
6.2. Results and Discussion.....	119

6.2.1. Stress Relaxation Test.....	119
6.2.2. Uniaxial Cyclic Deformation Tests.....	123
6.3. Summary and Conclusions.....	142
<b>7. Nanomechanics of <i>B. mori</i> Silk Fibroin-Hydroxyapatite Bio-Nanocomposite.....</b>	<b>144</b>
7.1. Nanoscale Atomistic Models of <i>B. mori</i> SF-HA bio-nanocomposite.....	145
7.1.1. Atomistic Computational Models of <i>B. mori</i> SF Nanostructure.....	145
7.1.2. Atomistic Computational Models of Hydroxyapatite Nanostructure.....	147
7.1.3. <i>B. mori</i> SF-HA bio-nanocomposite interface model.....	147
7.1.4. Atomistic computational model of <i>B. mori</i> SF-HA bio-nanocomposite.....	151
7.2. Simulation Details.....	153
7.2.1. Steered Molecular Dynamics Simulations.....	155
7.2.2. Tensile Test Simulations.....	156
7.3. Results and Discussion.....	157
7.3.1. Insights from Steered Molecular Dynamics Simulations of <i>B. mori</i> SF-HA Bio-nanocomposite Interface Model.....	158
<i>SF-HA Interface Debonding Mechanism</i> .....	163
<i>Variation in Potential Energy of SF-HA Interfaces</i> .....	165
<i>Role of Interfacial Interactions in SF-HA Interface Deformation Mechanics</i> .....	167
7.3.2. Insights from Molecular Dynamics Simulations for Tensile Test of <i>B. mori</i> SF-HA bio-nanocomposite Atomistic Model.....	172
<i>Potential Energy and Interatomic Interaction Energies in <i>B. mori</i> SF-HA Composite</i> .....	180
<i>Role of Peptide-Peptide and Peptide-HA Interaction Energies</i> .....	184
7.4. Summary and Conclusions.....	186
7.4.1. <i>B. mori</i> SF-HA interface.....	187
7.4.2. <i>B. mori</i> SF-HA bio-nanocomposite.....	188
<b>8. Conclusions and Contributions.....</b>	<b>190</b>
8.1. Conclusions.....	190
8.2. Contributions.....	193

8.3. Outlook.....195  
8.4. Future Work.....197  
References.....198  
List of Publications.....212

## List of Figures

<b>Figure 1.1:</b> Different types of biomaterials.....	2
<b>Figure 1.2:</b> Hierarchical structure of <i>B. mori</i> Silk Fiber. (a) <i>B. mori</i> silkworm cocoon. (b) <i>B. mori</i> silk fiber consists of two fibroin fibers forming the core coated with sericin protein holding the core fibers together. (c)The fibroin fibers consist of numerous nano-fibrils. (d) $\beta$ -sheet crystallite of size around 20X20X20 Å and (e) Amorphous chain.....	4
<b>Figure 1.3:</b> Atomistic representation of amino acid residues (a) Glycine, (b) Alanine, and (c) Serine.....	6
<b>Figure 1.4:</b> Silk Fibroin-hydroxyapatite bio-nanocomposite scaffold morphologies for bone tissue engineering applications.....	7
<b>Figure 3.1:</b> Schematic representation of fine organization of the primary structure of <i>B. mori</i> SF heavy chain, showing the 12 repetitive and 11 amorphous regions, respectively. An approximate amino acid sequence of the R10 region is illustrated by modules i, ii, and iii. Module iv depicts a typical amino acid sequence in the amorphous region. (Reprinted with permission from ref. [1]. Copyright 2005 American Chemical Society).....	18
<b>Figure 3.2:</b> Structural arrangement of (a) Parallel and (b) Anti-parallel $\beta$ -sheets.....	18
<b>Figure 3.3:</b> Building blocks of SF molecule. (a) $\beta$ -sheet crystallite consisting of 5 $\beta$ -sheets. (b) Single $\beta$ -sheet consisting of five $\beta$ – strands (hexapeptides). (c) All atom structure of one hexapeptide GAGAGS (forming the $\beta$ – strand). The residues displayed in blue, green, yellow represent Glycine, Alanine and Serine residues, respectively. (d) Amorphous chain used for creating SF model.....	20
<b>Figure 3.4:</b> 2D schematic representation the four hypothesized phenomenological models of <i>B. mori</i> SF nanostructure (a) I-NC; (b) II-CA; (c) III-AA; (d) IV-AACA.....	22
<b>Figure 3.5:</b> Variation of (a) Potential energy during minimization of model IV-AACA. (b) Energy switching function as a function of cut-off radius.....	26
<b>Figure 3.6:</b> (a) Energy vs. Time plot for equilibration simulation of model IV-AACA. During the 5ns NPT equilibration simulation, the total energy of the system is observed to decrease and then become constant showing a stable configuration of the system. (b and c) The volume/size of the simulation cell is also observed to decrease from 69X69X98 Å to 71X71X75 Å and thereafter becomes constant.....	28
<b>Figure 3.7:</b> Three dimensional schematic of the model IV-AACA along with the atomic model. Tensile deformation is applied along the fiber axis direction which, in this case, is aligned along the Z-axis.....	28

**Figure 3.8:** Stress-strain plots of the four models I-NC, II-CA, III-AA and IV-AACA at different strain rates, (a)  $5 \times 10^{-4}$  per fs, (b)  $5 \times 10^{-5}$  per fs, (c)  $5 \times 10^{-6}$  per fs, (d) Normal, shear and equivalent stress for model IV-AACA at  $5 \times 10^{-6}$  per fs strain rate. (e) Schematic diagram for stress-strain curve showing four distinct regimes.....32

**Figure 3.9:** Snapshots of the models IV-AACA, III-AA, II-CA and I-NC at different strain levels during deformation at strain rate of  $5 \times 10^{-6}$  per fs.....33

**Figure 3.10:** Comparison of the stress-strain plot for *B. mori* silk fibroin single filament of  $\sim 10 \mu\text{m}$  in diameter (Shao and Vollrath, 2002), *B. mori* silk fibre (degummed cocoon silk) of  $\sim 12 \mu\text{m}$  in diameter (Guo et al., 2017) and stress-strain plot obtained for the model IV-AACA at  $5 \times 10^{-6}$  per fs strain rate from MD simulation in present study.....36

**Figure 3.11:** Snapshots from deformation trajectory of model IV-AACA at (a) 0 strain and (b) 0.13 strain (yield point) at  $5 \times 10^{-6}$  per fs strain rate, uncoiling/stretching of amorphous chains is observed as highlighted, with no noticeable deformation in crystalline domain.....38

**Figure 3.12:** (a) Variation in number of H-bonds with increasing strain for model IV-AACA during the tensile deformation at different strain rates,  $5 \times 10^{-6}$  per fs,  $5 \times 10^{-5}$  per fs and  $5 \times 10^{-4}$  per fs. (b) Variation of energy with strain for model IV-AACA during the tensile deformation at  $5 \times 10^{-6}$  per fs strain rates.....39

**Figure 3.13:** Snapshots of the models at the start of strain hardening regime (a)IV-AACA, (b)III-AA, (c)II-CA at strain rate of  $5 \times 10^{-6}$  per fs, respectively. (d) Stress-strain plot of the four models at  $5 \times 10^{-6}$  per fs strain rate demarcating the start of strain hardening regime.....40

**Figure 3.14:** Snapshot of the crystalline region of model IV-AACA at 0.5 strain (50%) at  $5 \times 10^{-6}$  per fs strain rate, at this point  $\beta$ -strands start to slip out of the crystallites. Until this point the crystalline region still retains its structural integrity but the slip-out of  $\beta$ -strands mark the initiation of distortion in crystallites.....42

**Figure 3.15:** Snapshots of deformation trajectory of model IV-AACA at 0.5 strain (50%).....43

**Figure 3.16:** (a) Variation in in non-bonded energy with strain for crystalline region, Amorphous-L chains and Amorphous-P chains for model IV-AACA during the tensile deformation at strain rate  $5 \times 10^{-6}$  per fs. (b) Variation in non-bonded interaction energy between crystalline and Amorphous-L chains and crystalline and Amorphous-P chains for model IV-AACA during the tensile deformation at strain rate  $5 \times 10^{-6}$  per fs.....43

**Figure 3.17:** Snapshots of  $\beta$ -sheet crystallite of model IV-AACA at 1.3 strain. The crystallites are observed to be significantly distorted.....44

**Figure 3.16:** Snapshots of the models at start of fracture regime (a)IV-AACA, (b)III-AA, (c)II-CA, (d)I-NC at strain rate of  $5 \times 10^{-6}$  per fs and (e) Stress-strain plot of the four models at  $5 \times 10^{-6}$  per fs demarcating the start of fracture regime.....46

**Figure 3.17:** (a) Elastic modulus, (b) Tensile Strength and (c) Yield strain of the four models at different strain rates.....48

**Figure 3.18:** Variation in bonded and non-bonded energy with strain for model IV-AACA during the tensile deformation at two strain rates  $5 \times 10^{-5}$  per fs and  $5 \times 10^{-6}$  per fs.  $E_b$  and  $E_{nb}$  represents bonded energy and non-bonded energy, respectively.....49

**Figure 3.21:** Snapshots of tensile deformation simulation trajectory of IV-AACA model at different strain levels in case of tensile deformation at  $5 \times 10^{-6}$  /fs and  $5 \times 10^{-4}$  /fs strain rate.....51

**Figure 3.22:** Atomistic representation *B. mori* SF nanostructure models of different sizes. The models are named based on number of crystallites in x, y and z directions, (a)  $1P_{1X,1Y,2Z}$  - single crystallite in x and y directions and 2 in z-direction, (b)  $2P_{1X,2Y,2Z}$  - single crystallite in x direction and 2 in y and z-directions, (c)  $2P_{2X,2Y,2Z}$  - 2 crystallites in all the three directions, and (d)  $3P_{2X,2Y,3Z}$  - 2 crystallites in x and y directions and 3 in z-direction....53

**Figure 3.23:** Snapshots of tensile deformation trajectory of three *B. mori* SF nanostructure models of different sizes, at different strain levels during deformation at strain rate of  $5 \times 10^{-6}$  per fs.....54

**Figure 3.24:** Stress vs Strain plot for *B. mori* SF nanostructure models of different sizes, at strain rate of  $5 \times 10^{-6}$  /fs.....54

**Figure 4.1:** Schematic illustration of *B. mori* SF nanostructure and computational models based on the relative arrangement between amorphous and crystalline regions. (a) *B. mori* silk fiber comprising of two fibroin fibers and sericin coat. The fibroin fibers are a combination of several nano-fibrils. (b) The nano-fibril has numerous molecular chains forming  $\beta$ -sheet crystallites distributed in disordered domain made of amorphous segments. Two possible and distinct relative arrangements, (c) Parallel model; (d) Staggered model. (e) The  $\beta$ -sheet crystallites consist of 5 anti-parallel  $\beta$ -sheets, where each (f)  $\beta$ -sheet consists of 5  $\beta$  - strands. The residues shown in yellow, blue, and red represent Serine, Alanine and Glycine residues, respectively. (g) Amorphous chain employed for modelling the disordered domain of *B. mori* SF nanostructure.....60

**Figure 4.2:** Atomistic representation of the two hypothesized models of *B. mori* SF nanostructure in hydrated condition (a) Parallel model; (b) Staggered model.....62

**Figure 4.3:** Atomistic representation of the two hydration cases (a) 15 % hydration level and (b) 70 % hydration level of Parallel model before and after NPT equilibrium and the variation of kinetic energy, potential energy and total energy during the equilibration simulation. During the NPT equilibration simulation, the total energy of the system is observed to decrease and then become constant showing a stable configuration of the system. Also, after equilibration, the size of the simulation cell is observed to decrease for 15 % hydration whereas increase for 70 % hydration case. (c) Radial distribution of water molecules around serine and alanine residues in 70 % hydration case.....64

**Figure 4.4:** 3-dimensional schematic showing MD test setup for tensile deformation. Tensile deformation test is performed along the direction of fiber axis. The fiber axis here, is oriented along the Z-axis. Tensile deformation is attained by pulling a group of atoms on both the ends (as illustrated in grey boxes) of simulation cell with a constant velocity in opposite directions.....66

**Figure 4.5:** Stress vs Strain plot for (a) Parallel model at strain rate of  $5 \times 10^{-6}$  /fs, (b) Parallel model strain rate of  $5 \times 10^{-7}$  /fs and (c) Staggered model at strain rate of  $5 \times 10^{-6}$  /fs and (d) Staggered model at strain rate of  $5 \times 10^{-7}$  /fs, at varying hydration levels.....68

**Figure 4.6:** Variation in mechanical properties of Parallel and Staggered model with varying hydration level at two strain rates  $5 \times 10^{-6}$  and  $5 \times 10^{-7}$  /fs. (a, b) elastic modulus, (c, d) tensile strength and (e, f) yield strain of Parallel and Staggered models, respectively...70

**Figure 4.7:** Snapshots of a section of Parallel model at yield strain for 15%, 30%, 50% and 70% hydration cases. For lower hydration levels the water molecules are mostly present on the outer surface of the protein and with increase in hydration the amount of water molecules in the inter-chain spaces of polypeptide stands increases.....73

**Figure 4.8:** Crystalline region of Parallel model for unhydrated, 15% and 70% hydration cases. The amorphous chains and water molecules of the two models have been hidden for clarity. The crystallites in 70% hydrated model are seen to be exfoliated/swelled. That is, the gap between the  $\beta$ -sheets and  $\beta$ -strands for 70% hydration case is larger as compared to unhydrated and 15% hydration cases.....73

**Figure 4.9:** Snapshots of Parallel model for unhydrated case, 15%, 30% and 70% hydration cases at the strain corresponding to start of strain hardening regime. For hydrated cases, lesser uncoiling in amorphous chains is seen as compared to unhydrated case. Also, with deformation, the water molecules gather around the crystallites and crystalline-amorphous interface.....74

**Figure 4.10:** Snapshots of deformation simulation trajectory for Parallel model for unhydrated, 30% and 70% hydration cases at strain corresponding to end of failure regime. For hydrated cases it is seen that, most of the water molecules are concentrated around the crystalline region and the interface of amorphous and crystalline region. Also, with increase in hydration the distortion in crystallite is reducing as the  $\beta$ -strands are almost

non-interacting with each other hence little participation in load bearing resulting into weakening effect.....75

**Figure 4.11:** Variation in number of H-bonds in Parallel and Staggered models as a function of strain during tensile deformation at  $5 \times 10^{-6}$  /fs strain rate. (a) Peptide-peptide H-bonds and (b) Peptide-water H-bonds, for Parallel model, and similarly, variation in (c) Peptide-peptide H-bonds and (d) Peptide-water H-bonds as a function of strain, for Staggered model.....77

**Figure 4.12:** Snapshots of Parallel model for 50% hydration level in (a) undeformed state (0 strain) and (b) at  $\sim 1.3$  strain. During deformation, in higher hydration cases, the water molecules are seen to be moving out of the inter-chain spaces between the polypeptide strands in amorphous domain (or localized decrease in water density at various locations) and concentrate around the crystallites, resulting into a decrease in number of peptide-water H-bonds.....78

**Figure 4.13:** Variation in potential energy of protein for (a) Parallel and (b) Staggered model with increase in hydration levels. The potential energy of the protein in hydrated models is defined as the sum of the bonded and nonbonded energies of the protein part only, in its equilibrium state.....79

**Figure 4.14:** Variation in peptide-peptide interaction energies for Parallel model at varying hydration levels during tensile deformation at strain rates of  $5 \times 10^{-6}$  /fs and  $5 \times 10^{-7}$  /fs. (a, b) peptide-peptide non-bonded interaction energy, and (c, d) peptide-peptide bonded interaction energy, at  $5 \times 10^{-6}$  /fs and  $5 \times 10^{-7}$  /fs strain rates, respectively.....81

**Figure 4.15:** Variation in peptide-peptide interaction energies for Staggered model at varying hydration levels during tensile deformation at strain rates of  $5 \times 10^{-6}$  /fs and  $5 \times 10^{-7}$  /fs. (a, b) peptide-peptide non-bonded interaction energy, and (c, d) peptide-peptide bonded interaction energy, at  $5 \times 10^{-6}$  /fs and  $5 \times 10^{-7}$  /fs strain rates, respectively.....82

**Figure 4.16:** Variation in peptide-water interaction energy for (a, b) Parallel and (c, d) Staggered model at varying hydration levels during tensile deformation at strain rates of  $5 \times 10^{-6}$  /fs and  $5 \times 10^{-7}$  /fs, respectively.....83

**Figure 5.1:** Atomistic models of *B. mori* SF nanostructure. (a) Parallel model and (b) Staggered model.....89

**Figure 5.2:** Tensile deformation simulation setup. Tensile deformation is applied along the fiber axis direction which, in this case, is aligned along the Z-axis. Tensile deformation is achieved by moving a group of atoms on both the ends of simulation cell (as illustrated in grey boxes) with a constant velocity in opposite directions.....92

**Figure 5.3:** Snapshots of Parallel model, in case of 15% and 50% solvent content at 4.5M concentration, at different strain levels during deformation at strain rate of  $5 \times 10^{-6}$  per fs..94

**Figure 5.4:** Snapshots of Staggered model, in case of 15% and 50% solvent content at 4.5M concentration, at different strain levels during deformation at strain rate of  $5 \times 10^{-6}$  per fs.....94

**Figure 5.5:** Stress vs Strain plot obtained from tensile deformation of Parallel and Staggered models at  $5 \times 10^{-6}$  /fs strain rate, for 15, 30 and 50% of solvent contents of 0, 0.15, 1.5, 3 and 4.5 M saline solution. (a), (c) and (e) Parallel model in case of 15, 30 and 50% of solvent contents, respectively and (b), (d) and (f) Staggered model in case of 15, 30 and 50% of solvent contents, respectively.....95

**Figure 5.6:** Mechanical properties obtained for Parallel model and Staggered model with 15, 30 and 50% of solvent contents of 0, 0.15, 1.5, 3 and 4.5 M saline. (a and b) elastic modulus, (c and d) peak stress and (e and f) yield strain for Parallel and Staggered models, respectively.....96

**Figure 5.7:** Snapshots of simulation trajectory in case of Parallel model at 15% saline content of 1.5M concentration, at different strain levels, here the water molecules and salt ions are hidden for clear comprehension of *B. mori* SF nanostructure. *B. mori* SF nanostructure (a) in undeformed state, (b) at yield point, i.e., at 0.14 strain, represent the structure in elastic regime, (c) at 0.6 strain, representative nanostructure in strain softening regime, (d) 1.2 strain and (e) at 1.7 strain, representative nanostructure in strain hardening regime. VMD snapshot of a section of (f) crystalline and (g) amorphous domains before deformation, at  $\sim 0.16$ , 0.6 and 1.2 strain levels.....100

**Figure 5.8:** Number of H-bonds and peptide-peptide non-bonded interaction energy vs strain during tensile deformation in case of Parallel model. (a) Peptide-peptide H-bonds for 30% saline content of 0, 0.15, 1.5, 3 and 4.5M salt concentration, (b) Peptide-peptide H-bonds for 15, 30 and 50% saline content of 4.5M salt concentration, (c) and (d) Peptide-peptide non-bonded interaction energies for 30% and 50% saline content, respectively, of 0, 0.15, 1.5, 3 and 4.5M salt concentration.....102

**Figure 5.9:** Snapshots of Parallel model in case of 4.5M, 15% saline content, showing (a) and (b) Peptide-Salt-Peptide inter-chain ionic bridge connecting two peptide strands (shown in blue and color) and (c) Peptide-Salt-Peptide intra-chain ionic bridge connecting two segments within the same polypeptide chain.....104

**Figure 5.10:** Snapshots of simulation trajectory for Parallel model in case of 4.5M, 50% saline content, (a) in undeformed state (before stretching), (b) at  $\sim 1.2$  strain. For higher salt content, larger aggregates of NaCl is observed which distort during tensile stretching process contributing significantly to enhanced mechanical response observed, which can be seen in (c) and (d) stress-vs strain for Parallel model in 4.5M saline environment at 15% and 50% solvent content, respectively, showing the total stress and the amount of stress components developed in the three constituents of the system, i.e., protein, salt and water.....105

**Figure 5.11:** Number of Peptide-salt contacts vs saline concentration in case of (a) Parallel and (b) Staggered models with 15, 30 and 50% saline content of 0, 0.15, 1.5, 3 and 4.5M salt concentrations. (c) and (d) Snapshots of Parallel model with 4.5M saline at 15% and 50% contents, respectively, showing the salt ions forming coulombic contacts with atoms in peptide chains, i.e., the salt ions within 3Å of atoms in polypeptide chain (rest of the salt ions, having more than 3Å distance from polypeptide chains, are hidden for clarity).....106

**Figure 5.12:** Number of peptide-salt coulombic contacts vs strain during tensile deformation in case of Parallel (a, c, e) and Staggered models (b, d, f) for 15%, 30% and 50% of solvent contents of 0, 0.15, 1.5, 3 and 4.5 M saline solution.....108

**Figure 5.13:** VMD snapshot of Parallel model at (a) 15% solvent content and (b) 50% solvent content of 4.5M concentration, showing x, y, and z dimensions. Here the water molecules and salt ions are hidden for clarity. (c) RMSD plot for Parallel and Staggered models at 15% and 50% solvent content of 4.5M concentration. VMD snapshots of deformation simulation trajectory in case of (d) and (g) Parallel and (e) and (h) Staggered model at 50 % saline content of 4.5M concentration, in undeformed state and at ~0.5 strain. (f) Radial distribution plot of Na<sup>+</sup> ions around the oxygen atoms present in *B. mori* SF nanostructure for Parallel and Staggered models at 50% solvent content of 4.5M concentration.....110

**Figure 5.14:** Evolution of peptide-salt interaction during tensile deformation process in case of Parallel model (a, c, e) and Staggered model (b, d, f) for 15%, 30% and 50% of solvent contents of 0, 0.15, 1.5, 3 and 4.5 M saline solution.....113

**Figure 6.1:** Uniaxial cyclic deformation simulation setup. Cyclic deformation is applied along the fiber axis direction which, in this case, is aligned along the z-axis. Cyclic deformation is achieved by constraining a group of atoms, at one extreme of simulation cell (as highlighted by the grey boxes at the left side, along z direction), to a fixed position, and simultaneously, moving a group of atoms at opposite extreme of simulation cell (as highlighted by the grey boxes at the right side in z direction), with a sinusoidally changing velocity.....117

**Figure 6.2:** Stress vs time curves obtained from stress relaxation test of Parallel model in (a) anhydrous condition, at (b) 15% hydration level, (c) 50% hydration level and (d) relaxation modulus plot for stress relaxation test of Parallel model in anhydrous condition. ....121

**Figure 6.3:** Snapshot of stress relaxation simulation trajectory (a) before and (b) after relaxation in case of Staggered model in anhydrous conditions. Unwinding and stretching of polypeptide chains, as highlighted by black colored chain segments and conformational changes of polypeptide chains, as highlighted by yellow and magenta colored chain segments, is observed. (c) and (d) Timeline analysis of secondary structure evolution of

yellow and magenta colored chains, respectively, during 5ns of stress relaxation.  
.....122

**Figure 6.4:** Stress and strain vs time curve (in anhydrous condition) and stress-strain hysteresis loop (for varying hydration conditions) of Parallel model, in case of (a, d) 1.5%, (b, e) 2.5% and (c, f) 6% strain amplitude.....125

**Figure 6.5:** Stress and strain vs time curve (in anhydrous condition) and stress-strain hysteresis loop (for varying hydration conditions) of Staggered model, in case of (a, d) 1.5%, (b, e) 2.5% and (c, f) 6% strain amplitude.....126

**Figure 6.6:** Snapshot of cyclic deformation simulation trajectory in case of Parallel model in anhydrous conditions, (a) before deformation, (b) at the end of 2<sup>nd</sup> tension-compression cycle, and (c) at the end of 5<sup>th</sup> tension-compression cycle. Change in the conformation of polypeptide chains during cyclic deformation is highlighted by black colored chain segments. (d) Timeline calculation plot for the secondary structure of 1/8<sup>th</sup> section of Parallel model of *B. mori* SF nanostructure, before and after cyclic deformation simulation. (e) Timeline calculation plot for the secondary structure evolution of single amorphous chain present in *B. mori* SF nanostructure, during cyclic deformation simulation (Parallel model).....127

**Figure 6.7:** Stress-strain hysteresis loop obtained from cyclic deformation tests of Parallel model at (a) 6%, (b) 2.5% and (c) 1.5% strain amplitude and Staggered model at (d) 6%, (e) 2.5% and (f) 1.5% strain amplitude, in anhydrous condition.....130

**Figure 6.8:** Stress-strain hysteresis loop for Parallel model in (a) anhydrous condition and at (b) 15, and (c) 50% of hydration levels and Staggered model in (d) anhydrous condition and at (e) 15, and (f) 50% of hydration levels, obtained from cyclic deformation tests at 6% strain amplitude.....133

**Figure 6.9:** Variation of potential energy and individual energy components as a function of time for (a) Parallel and (b) Staggered models, during the cyclic deformation test at 6% strain amplitude and at 15% hydration level.....133

**Figure 6.10:** Comparison of storage modulus values for Parallel model obtained from cyclic deformation simulations, in case of 1.5%, 2.5% and 6% strain amplitudes and the instantaneous modulus obtained from relaxation simulation.....134

**Figure 6.11:** Effect of input strain amplitude, frequency, and deformation cycles on viscoelastic behaviour and damage accumulation in *B. mori* SF nanostructure. Variation of loss factor as a function of strain amplitude for (a) Parallel and (b) Staggered model. (c) Variation of loss factor vs frequency of deformation cycle. (d) Schematic stress vs strain hysteresis plot showing inelastic strain range. Variation of inelastic strain as a function of deformation cycle for (e) Parallel and (f) Staggered model.....136

<b>Figure 6.12.</b> Variation of loss factor values as a function of deformation cycle for Parallel and Staggered model.....	137
<b>Figure 6.13:</b> Variation of potential energy and individual energy components as a function of time for (a) Parallel and (b) Staggered models, during the cyclic deformation test at 6% strain amplitude and at 15% hydration level.....	139
<b>Figure 6.14.</b> Snapshot of cyclic deformation trajectory in case of Parallel model in 15% hydration, (a) before deformation, and (b) at the end of cyclic deformation.....	141
<b>Figure 6.15.</b> Snapshot of single crystallites before and after cyclic deformation in case of (a and b) Parallel model and (c and d) Staggered model, in case of 15% water content....	142
<b>Figure 7.1:</b> Atomistic models of <i>B. mori</i> SF nanostructure. (a) Parallel model and (b) Staggered model. ....	146
<b>Figure 7.2:</b> Atomistic model of hydroxyapatite consisting of 8 unitcells.....	147
<b>Figure 7.3:</b> Atomistic model of <i>B. mori</i> SF–hydroxyapatite interface. (a) SEM image of electrospun SF-HA scaffolds [4], (b) TEM images of SF-HA composite fibers [5], (c) Schematic representation of <i>B. mori</i> SF fiber with Hap particle deposited on its surface, (d) Atomistic model of SF–HA interface....	148
<b>Figure 7.4:</b> Schematic representation of SF–HA interface models, in <i>B. mori</i> SF-HA bio-nanocomposite, with two chemically different surfaces of (a) HA block in contact with SF phase forming (b) OH-SF interface, and (c) Ca-SF interface.....	149
<b>Figure 7.5:</b> SF–HA interface models, in <i>B. mori</i> SF-HA bio-nanocomposite, with HA block thickness of (a) ~1.8 nm, (b) ~3.6 nm, and (c) ~5.4 nm thickness.....	150
<b>Figure 7.6:</b> Schematic representation of <i>B. mori</i> SF-HA nanocomposite fiber with HA particle deposited on SF surface, (b) Atomistic model of SF–HA bio-nanocomposite...	152
<b>Figure7.7:</b> Atomistic models for <i>B. mori</i> SF-HA bio-nanocomposite for HA contents of (a) 10%, (b) 20%, (c) 30%, and (d) 40% v/v. ....	153
<b>Figure 7.8:</b> Simulation set-up for SMD simulation of SF-HA interface, showing fixed group of atoms in HA block (in black), SMD atom in SF phase (in blue), i.e., the atoms being pulled with spring and the spring attached to the center of mass of the SMD atoms which is then pulled with constant velocity. ....	155
<b>Figure 7.9:</b> MD test setup for tensile deformation of <i>B. mori</i> SF-HA bio-nanocomposite models. Tensile deformation test is performed along the direction of fiber axis of SF phase.	

The fiber axis here, is oriented along the Z-axis. Tensile deformation is attained by pulling a group of atoms in SF phase on both the ends (as illustrated in grey boxes) of simulation cell with a constant velocity in opposite directions.....157

**Figure 7.10:** Snapshots of SMD simulation trajectory for Parallel model in case of OH-SF and Ca-SF interfaces, for 1L thickness, at various stages of deformation..... 159

**Figure 7.11:** Snapshots of SMD simulation trajectory for Staggered model in case of OH-SF and Ca-SF interfaces, for 1L thickness, at various stages of deformation. .... 160

**Figure 7.12:** Force vs Displacement plots for Parallel model in case of (a) OH-SF interface and (b) Ca-SF interface, and for Staggered model in case of (c) OH-SF interface and (d) Ca-SF interface. (e) Force vs Displacement plot showing different regimes of deformation. ....161

**Figure 7.13:** Variation in potential energy for Parallel and Staggered models in case of 1L thickness of HA phase, during SMD simulation. (a) OH-SF interface and (b) Ca-SF interface, for Parallel model, and similarly, (c) OH-SF interface and (d) Ca-SF interface, for Staggered model.....155

**Figure 7.14:** Variation in number of SF-HA electrostatic contacts in Parallel and Staggered models as a function of displacement during SMD simulation in case of (a) OH-SF interface and (b) Ca-SF interface, for Parallel model, and similarly, (c) OH-SF interface and (d) Ca-SF interface, for Staggered model.....168

**Figure 7.15:** Snapshots of SMD simulation trajectory for Parallel model, in case of (a) OH-SF and (b) Ca-SF interfaces, for 1L thickness, at large deformations. The snapshots show the SF-HA interface models in 3 dimensional orientation obtained by rotating the models about z axis. During the peel-off simulation, even at large deformation some of the peptide strands are seen to be still sticking to the surface of HA block in contact with SF phase. .... 169

**Figure 7.16:** Variation in peptide-HA interaction energy for Parallel and Staggered models in case of all the three thicknesses of HA phase, during SMD simulation. (a) OH-SF interface and (b) Ca-SF interface, for Parallel model, and similarly, (c) OH-SF interface and (d) Ca-SF interface, for Staggered model..... 170

**Figure 7.17:** Snapshots of simulation trajectory for Parallel model in case four HA contents, (a) and (b) shows the snapshots for 10% HA content case, (c) and (d) for 20% HA content case, (e) and (f) for 30% HA content case, and (g) and (h) for 40% HA content case. The deformation is seen to originate from uncoiling and stretching of amorphous chains, at non-bonded interface in SF phase, and in amorphous chains towards the right end of SF phase, for lower and higher HA contents, respectively, and void formation in SF phase, followed by shear deformation of crystalline domain..... 174

**Figure 7.18:** Snapshots of simulation trajectory for Staggered model in case four HA contents, (a) and (b) shows the snapshots for 10% HA content case, (c) and (d) for 20% HA content case, (e) and (f) for 30% HA content case, and (g) and (h) for 40% HA content case. In Staggered model also, similar to Parallel model, the deformation originates from uncoiling and stretching of amorphous chains, resulting into void formation in SF phase, followed by shear deformation of crystalline domain. However, in Staggered model a more uniform deformation, as compared to Parallel model, is seen.....175

**Figure 7.19:** Stress vs Strain plot for (a) Parallel model, and (b) Staggered model in case of 10, 20, 30 and 40% HA contents v/v. Variation in mechanical properties of Parallel and Staggered model with varying HA content along with the mechanical properties predicted from Halpin Tsai model for the four HA contents, (c) elastic modulus, and (d) tensile strength and (e) Yield Strain.....176

**Figure 7.20:** Variation in potential energy and various interaction energies for Parallel and Staggered models, during tensile deformation. (a and c) Potential energy variation as a function of strain in case of 20% and 40% HA content, respectively for Parallel model. (b and d) Similarly, corresponding plots for Staggered model. Variation of different interaction energies and total non-bonded energy as a function of strain in case of (e and g) 20% and 40% HA content, respectively, for Parallel model, and similarly, (f and h) corresponding plots for Staggered model. Here, peptide-peptide interactions, peptide-HA interactions, and non-bonded interactions among atoms in HA phase are denoted as PP, PH and HH, respectively.....182

**Figure 7.21:** Variation in peptide-peptide and peptide-HA interaction energies for Parallel and Staggered models, during tensile deformation. Peptide-peptide interaction energy as a function of strain for (a) Parallel model and (b) Staggered model, in case of all the four HA contents. Peptide-HA interaction energy as a function of strain for (a) Parallel model and (b) Staggered model, in case of all the four HA contents.....185

**Figure 7.22:** Snapshots of deformation trajectory for Parallel model in case of 40% HA content. During tensile deformation, at large strain values, as the crystallites in SF phase deform, some of the  $\beta$ -strands from the crystalline region, move towards to HA block, increasing the peptide-HA interaction. ....186

## List of Tables

<b>Table 1.1:</b> Mechanical properties of <i>B. mori</i> SF and other biomaterials.....	9
<b>Table 3.1:</b> Comparison of tensile properties of the four <i>B. mori</i> SF nanostructure models at different strain rates obtained in present work, and the values for silk fiber reported elsewhere.....	34
<b>Table 3.2:</b> Comparison of mechanical properties obtained for <i>B. mori</i> SF nanostructure models of different sizes.....	55
<b>Table 6.1:</b> Relaxation time for Parallel and Staggered models in anhydrous condition and at 15, 30 and 50 % of hydration levels.....	120
<b>Table 6.2:</b> Loss factor for Parallel and Staggered models obtained from complex modulus expression for a standard linear viscoelastic material.....	124
<b>Table 6.3:</b> Dynamic mechanical properties of Parallel model of <i>B. mori</i> SF nanostructure under cyclic loading. The storage and loss modulus values are in GPa.....	132
<b>Table 6.4:</b> Dynamic mechanical properties of Staggered model of <i>B. mori</i> SF nanostructure under cyclic loading. The storage and loss modulus values are in GPa.....	132
<b>Table 7.1:</b> Rupture force required for deformation of SF–HA interface for both Parallel and Staggered models, in case of OH-SF and Ca-SF interface and three different thicknesses.....	162
<b>Table 7.2:</b> Maximum shear stress at SF–HA interface both Parallel and Staggered models, in case of OH-SF and Ca-SF interface and three different thicknesses.....	163
<b>Table 7.3:</b> Elastic modulus values for matrix ( <i>B. mori</i> SF) and filler (HA), $\eta$ and geometry parameter values utilized to predict elastic modulus values for composite ( <i>B. mori</i> SF-HA bio-nanocomposite) using Halpin-Tsai model.....	173